CRYSTAL GROWTH & DESIGN

Article

pubs.acs.org/crystal

Influence of (Al, Fe, Mg) Impurities on Triclinic Ca_3SiO_5: Interpretations from DFT Calculations

Jian Huang,[†,⊥] Loredana Valenzano,[‡] Tajendra Vir Singh,[∥] Ravindra Pandey,[§] and Gaurav Sant*[,†,⊥]

[†]Laboratory for the Chemistry of Construction Materials (LC^2), Department of Civil and Environmental Engineering, University of California, Los Angeles, California 90095-1593, United States

[‡]Department of Chemistry and [§]Department of Physics, Michigan Technological University, Houghton, Michigan 49931, United States

[∥]HPC Research and Projects, Institute for Digital Research and Education (IDRE), University of California, Los Angeles, California 90095-1557, United States

[⊥]California Nanosystems Institute (CNSI), University of California, Los Angeles, California 90095, United States

Supporting Information

ABSTRACT: Ca_3SiO_5 and its polymorphic representations are the dominant phase(s) present in ordinary portland cement (OPC). As environmental pressures bracket the production of OPC, there is increasing emphasis on designing newer, more efficient OPC chemistries. While minor impurities in the form of (Al, Fe, Mg) are long understood to have substantial influences on the structure and reactivity of the siliceous cementing phases, specific details at the atomistic level remain unclear. In this paper, we report the results of first-principles calculations performed at the density functional level of theory (DFT), on triclinic Ca_3SiO_5, a template phase of relevance to OPC doped with (Al, Fe, Mg) species. Focus is devoted toward understanding modifications induced in (a) the lattice and crystallographic parameters, (b) the mechanical properties, and (c) the electronic descriptors of the silicate. Special efforts are devoted to identify preferred atomic substitution sites and to rank the stability of different phases using thermochemical descriptors. The results suggest that the presence of (Al, Fe, Mg) impurities in the silicate lattice modifies charge localization and exchange, contributing a new means toward interpreting and steering cementing phase reactivity, by careful manipulations of their impurity distributions.

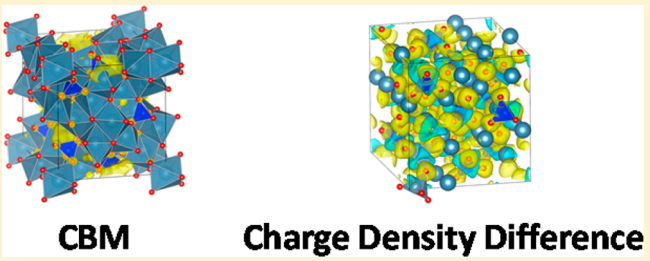

1. INTRODUCTION AND BACKGROUND

Second to water, concrete is the most widely used material on earth, a function of its low cost, excellent mechanical properties, and chemical durability.[1] However, the manufacture of the primary binding phase in concrete, ordinary portland cement (OPC), now accounts for around 6−9% of global CO_2 emissions.[2] For this reason, substantial efforts are being directed to reduce the CO_2 burden of cement production and consumption.[3] While special attention has been devoted to incorporating chemical and mineral additives in cement and optimizing concrete mixture proportions, few efforts have attempted to re-engineer portland cement as a binding material.[4] One very promising re-engineering strategy lies in improving cement reactivity by the controlled introduction of chemical impurities into the cementing phases. While it is empirically recognized that impurities influence the crystalline structure and the reactivity of the dominant siliceous cementing phases (i.e., Ca_3SiO_5 and Ca_2SiO_4), a fundamental understanding of their presence (i.e., of type or content) remains unclear.[4−10] This is significant because increasing phase reactivity is a means to achieve material sustainability by doing "more with less", that is, by using smaller quantities of *highly reactive OPC* to produce concretes with properties comparable to those produced today using a larger quantity of traditional OPC.

OPC consists of four major defective phases: Ca_3SiO_5 (50−70%), Ca_2SiO_4 (15−30%), $Ca_3Al_2O_6$ (5−10%), and $Ca_4Al_2Fe_2O_{10}$ (5−15%).[4] Among these, alite (i.e., impure, monoclinic tricalcium silicate, MIII-Ca_3SiO_5[11,12]) is a dominant constituent of technical cement clinkers, given its high hydraulic reactivity and ability for rapid strength gain. Ca_3SiO_5 assembles itself in different polymorphs according to temperature and impurity contents.[4] There are seven polymorphs of Ca_3SiO_5, including three triclinic (T), three monoclinic (M), and one rhombohedral (R) structure.[4] These polymorphs demonstrate (displacive) phase transitions induced by progressive deformations of the unit cell, where, for example, bond angles change more dramatically than bond lengths.[13] Dunstetter et al. reviewed the nature of polymorphism in Ca_3SiO_5.[14] They concluded that all polymorphs can be

Received: November 4, 2013
Revised: March 19, 2014
Published: April 11, 2014

   dx.doi.org/10.1021/cg401647f | Cryst. Growth Des. 2014, 14, 2158−2171

described in terms of the superstructures of the parent triclinic, monoclinic, and rhombohedral (T, M, R) unit cells as a result of the "displacive polymorphism" displayed by these structures. However, alite, the primary MIII-Ca_3SiO_5 polymorph present in technical OPC, is stable at room temperature only when doped with Mg and Al impurities.[4] As a consequence, it is difficult to experimentally ascertain the effects of impurity species on the reactivity of alite, since it is already impure at room temperature. On the other hand, phase-pure Ca_3SiO_5, which crystallizes in a triclinic lattice (i.e., TI-Ca_3SiO_5), is stable at room temperature and is amenable to impurity substitution.[6] For this crucial reason, the *crystallographically consistent template* of TI-Ca_3SiO_5 is chosen as an initial starting point to advance our understanding of the influences of impurities on cement phase structure and reactivity.

Recently, Manzano et al.[15] studied the influence of ionic substitutions on the structure, elastic properties, and electronic structures of alite (MIII-Ca_3SiO_5) and belite (β-Ca_2SiO_4) using force field and DFT methods. Their classical simulations indicated that impurities such as (Al, Fe, Mg) do not show preferred substitution sites. However, their DFT results showed that the chemical nature of the impurities has very different impacts on the electronic structure, in particular in terms of charge localization along the valence and conduction bands, which, in turn, influences reactivity. The conclusion that impurities in alite exert a more substantial effect on the charge localization than on crystallographic features was also confirmed by Durgun et al.[16] Given the lack of similar information for TI-Ca_3SiO_5, a *critical template phase*, this study for the first time applies DFT calculations to rigorously understand the influences of Mg^{2+}, Al^{3+}, and Fe^{3+} impurities on both its structural and electronic features. The results provide guidance on deconvoluting the role of impurities and bonding features in these phases, key information that is needed to synthesize highly reactive cements by careful manipulations of impurity species while limiting the number of trial-and-error cycles and impure compositions considered in experiments.

2. COMPUTATIONAL METHODOLOGY

The crystalline structure of TI-Ca_3SiO_5 (TI-C_3S) established by Golovastikov et al. was used as the initial starting point for our calculations.[17] TI-Ca_3SiO_5 belongs to the $\bar{P}_1$ space group and its unit cell contains 162 atoms with 83 irreducible atoms. As shown in Figure 1, the structure consists of an array of 18 $[SiO_4]^{4-}$ tetrahedra and 18 interstitial O sites. The tetrahedra include 72 O atoms wherein the 18 Si atoms constitute shared vertices for each of the three irregular Ca polyhedra. Among the 18 interstitial O sites, 17 O atoms serve as common vertices for six Ca octahedra, and the exceptional O atom only connects with five Ca polyhedra.[17] Starting from an optimized TI-Ca_3SiO_5 structure, where lattice parameters and atomic positions were allowed to relax, (Al, Fe, Mg) ions were systematically inserted into the TI-Ca_3SiO_5 lattice. In order to ensure charge balance, we introduced 1:1 substitutions of Mg for Ca, while Al and Fe insertions were made by simultaneously replacing one Ca and one Si atom with two Al or two Fe atoms in the positions of the former species.[4] In general, (Al, Fe, Mg) atoms replace Ca atoms at four highly symmetric points (0, 0, 0), (0.5, 0.5, 0.5), (0, 0.5, 0), and (0.5, 0, 0.5) (Figure 1). To investigate the influences of the site preference of impurities, an additional Mg, Al, or Fe impurity was inserted at the nearest, second-nearest, or third-nearest site to the initial high-symmetry substitution site. As such, the "third-nearest" site corresponds to a position nearest to the high-symmetry point (0.5, 0.5, 0.5). Since the second nearest site reflects characteristics similar to the nearest substitution site, these results are not presented; rather, distinct features relevant to the third-nearest atomic substitution site are discussed in detail. An illustration

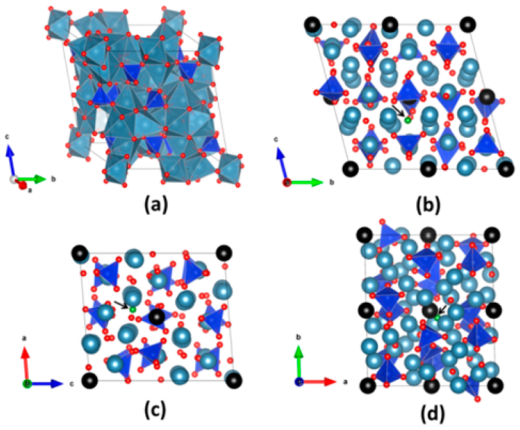

Figure 1. The crystal structure of TI-Ca_3SiO_5. (a) Si tetrahedra (blue), Ca polyhedra (gray), and O atoms (red) are shown. Various plane projections are shown: (b) {100} plane, (c) {010} plane, and (d) {001} plane. Thus, black spheres correspond to calcium atoms at four high-symmetry points: (0, 0, 0), (0, 0.5, 0), (0.5, 0, 0.5), and (0.5, 0.5, 0.5). The small green atom denoted with an arrow is the exceptional O atom, which is only connected to five Ca polyhedra.

of the substitutional scheme is shown in Figure ES1 (Supporting Information) and described below.

Case 1: Pure triclinic Ca_3SiO_5 (TI-Ca_3SiO_5) phase is the baseline representation.

Cases 2−6: Mg impurities are substituted at positions of Ca atoms, at the four high-symmetry points a, (0, 0, 0); b, (0.5, 0.5, 0.5); c, (0.5, 0, 0.5); and d, (0, 0.5, 0). In the case of single species substitutions, we compare cases 2 and 3, where Mg replaces Ca at "site a" and "site b", respectively. When double substitutions are made, we refer to cases 4 and 5, where sites a and b (case 4) and sites a and e (case 5) are occupied by Mg species. This would simulate scenarios wherein Mg impurities are located proximate to (case 5) and far away from (case 4) each other. Finally, for case 6, four independent Ca sites, i.e., a, b, c, d, are all substituted by Mg atoms.

Cases 7−10: Two Al atoms substitute simultaneously at Ca and Si sites. First, Al is inserted at a high-symmetry (0, 0, 0) Ca site and at the nearest Si position, i.e., site b (case 7) or at the third nearest Si site "site c" to the initially substituted Ca position (case 8). In case 7, two Al tetrahedra are connected by a bridging O atom, denoted as [Al]−O−[Al] wherein the parenthetical identifier "[...]" indicates a tetrahedron. As such, for case 8, the Ca−O−[Si] sites from case 1 are modified to correspond to Al−O−[Si] and Ca−O−[Al], respectively. Further, an Al insertion is carried out at another high-symmetry (0.5, 0.5, 0.5) Ca position ("site d") and at its nearest Si position, "site e". This corresponds to case 9, where [Al]−O−[Al] lies at the center of the crystal lattice. Finally, case 10 then combines the substitutions from cases 7 and 8 to introduce four Al atoms (i.e., two [Al]−O−[Al] formations) into an impure variant of TI-Ca_3SiO_5.

Cases 11 and 12: Both of these cases include two Al atoms and one Mg atom, for a total of three impurity atoms in the unit cell. As such, case 11 is a derivative of case 7 that includes an additional Mg substitution (for Ca) that is positioned nearest to a Si position site d. Next, case 12 is another derivative of case 7 that includes an additional Mg atom inserted at a Ca position at site c (0.5, 0.5, 0.5).

Cases 13−16: These cases consider Fe substitutions carried out similarly to those described for case 7. Here, the different cases account for different spin-polarized states of Fe species. More specifically, cases 13, 14, and 15 correspond to nonmagnetic, antiferromagnetic (AF), and ferromagnetic (FM) high-spin solutions, respectively. As such, case 13 is indicated as Fe−O−[Fe], and cases 14 and 15 correspond to [Fe]−O−[Fe]. Furthermore, case 16 is equivalent to the substitutions carried out in case 8, wherein antiferromagnetic solutions are imposed; this case corresponds to [Fe]−O−[Si] and Ca−O−[Fe], respectively.

dx.doi.org/10.1021/cg401647f | Cryst. Growth Des. 2014, 14, 2158−2171

Table 1. Structural and Thermochemical Properties of Pure and Impure TI-Ca_3SiO_5

	a (Å)	b (Å)	c (Å)	α (deg)	β (deg)	γ (deg)	volume (Å^3)	$\Delta H_{fo}/\Delta H_{fe}$ (kJ/mol)
Checkpoint 1								
DFT calculation	11.73	14.28	13.73	104.8	94.4	90.1	2215.4	−109.4/−2674.2
experiment	11.67	14.24	13.72	105.5	94.3	90.0	2192.1	−117.2/−2933.1[30]
E_{DFT} = 145.3 GPa, E_{EXP} = 135−147 GPa[33]				G_{DFT} = 57.7 GPa			K_{DFT} = 100.4 GPa	
Checkpoint 2								
DFT calculation	11.72	14.27	13.69	104.7	94.3	90.0	2209.5	−104.2/−2668.8
experiment	11.62	14.16	13.63	105.0	94.6	90.1	2157.2	–
E_{DFT} = 141.7 GPa, E_{EXP} = 125 GPa[33]				G_{DFT} = 56.2 GPa			K_{DFT} = 98.5 GPa	

All calculations were performed at the density functional level of theory (DFT) using the Quantum Espresso distribution.[18] A plane-wave basis and Vanderbilt ultrasoft pseudopotentials were used.[19] The Perdew−Wang (PW91) generalized gradient approximation (GGA) was adopted to treat exchange−correlation effects in the form of the PW91 functional.[20] Cutoffs of 816 and 8163 eV were imposed on the kinetic energy and charge density, respectively. Integration of the first Brillouin zone (BZ) was performed at the gamma point. The convergence accuracy on the total energy was set to 1.36×10^{-7} eV. Atomic relaxations were allowed when all structural optimizations were carried out. All the crystal structures were optimized using the Broyden−Fletcher−Goldfarb−Shannon (BFGS) scheme with a numerical threshold of 2.57×10^{-4} eV/Å.[21] To elucidate the role of magnetism, spin polarization in the form of both ferromagnetic (FM) and antiferromagnetic (AF) solutions was imposed when Fe impurities were introduced into TI-C_3S (i.e., TI-Ca_3SiO_5). Visualizations of all the structures and charges were performed using VESTA.[22]

The independent second-order tensorial components characterizing the elastic response of a triclinic lattice to mechanical stress were evaluated by applying small strains to the equilibrium structure. Eight values of strain (i.e., $\varepsilon = \pm 0.0025, \pm 0.0050, \pm 0.0075, \pm 0.0100$) were considered. The corresponding stress was fitted by a least-squares method. After a given strain was applied, in order to retrieve the necessary components of the elastic constants, the atomic coordinates were allowed to relax. The elastic constants were used to determine the bulk (K), shear (G), and elastic (E) moduli per the Reuss−Voigt−Hill (RVH) approximations.[23] Quantifications of the elastic constants are used to estimate the mechanical stability of the crystalline lattice under the due constraint that the 6×6 matrix describing the complete elastic tensorial components (C_{ij}) must be "positive definite".[24]

To provide an additional point of comparison to quantify the stabilities of pure/impure phases, the following thermochemical/energetic properties were addressed: (a) enthalpy of formation of a phase from its elements (ΔH_{fe}, eq 1) and simple oxides (ΔH_{fo}, eq 2) for phases represented by the generic composition $Ca_{(3-x-y-z)}Mg_xAl_{2y}Fe_{2z}Si_{(1-y-z)}O_5$ and (b) cohesive energy (E_C, or lattice energy) of all phases (eq 3):

$$\Delta H_{fe} = E_{tot} - (3 - x - y - z)E_{Ca} - xE_{Mg} - 2yE_{Al} - 2zE_{Fe} - (1 - y - z)E_{Si} - 2.5E_{O_2} \quad (1)$$

$$\Delta H_{fo} = E_{tot} - (3 - x - y - z)E_{CaO} - xE_{MgO} - yE_{Al_2O_3} - zE_{Fe_2O_3} - (1 - y - z)E_{SiO_2} \quad (2)$$

$$E_C = E_{tot} - (3 - x - y - z)E'_{Ca} - xE'_{Mg} - 2yE'_{Al} - 2zE'_{Fe} - (1 - y - z)E'_{Si} - 5E'_{O} \quad (3)$$

where E_{tot} is the total energy of the compound, E_{EL} is the energy of the elements (EL = Ca, Mg, Al, Fe, and Si) in the ground state, E_{O_2} is the energy of the oxygen dimer (eq 1), E_{ox} (ox = CaO, MgO, Al_2O_3, Fe_2O_3, and SiO_2) is the total energy of the corresponding oxides (eq 2), and E'_{atom} (atom = Ca, Mg, Al, Fe, Si, and O) is the energy of isolated Ca, Mg, Al, Fe, Si, and O atoms (eq 3). The X-ray diffraction (XRD) patterns of all phases were calculated for comparison with experiment (when available) for an incident beam corresponding to Cu Kα radiation using RIETAN or X'Pert HighScore Plus.[25] The first-principles-based GIPAW method was applied to compute solid-state magic angle spinning nuclear magnetic resonance (MAS NMR) parameters, including the chemical shielding tensors (σ), quadrupolar coupling constant (C_q), and asymmetry parameter (η).[26] Isotropic chemical shieldings were obtained as written by $\sigma_{iso} = \mathrm{Tr}[\sigma/3]$ and compared to experimental isotropic chemical shifts expressed as $\delta_{iso} = \sigma_{ref} - \sigma_{iso}$. $CaCl_2$ and $Si(CH_3)_4$ were used as the reference points for describing chemical shifts for ^{43}Ca and ^{29}Si MAS NMR spectra. All NMR spectra were processed using the SIMPSON distribution using calculated chemical shifts and quadrupolar parameters.[27]

3. RESULTS AND DISCUSSION

3.1. Pure and Impure TI-Ca_3SiO_5: Validation of the Crystallographic Template. To ensure the accuracy and reliability of the calculations, three independent checkpoints were established by comparison, when available, with experimental determinations of (a) the lattice parameters and X-ray diffraction data sets, (b) the enthalpies of formation, and (c) the mechanical properties in the form of elastic moduli. As such, the systems considered herein include (1) pure-phase TI-Ca_3SiO_5 and (2) TI-Ca_3SiO_5 containing Mg and Al impurities. The impure variant considered herein, i.e., of composition $Ca_{2.944}Mg_{0.037}Al_{0.037}Si_{0.981}O_5$, was chosen as *being similar*, but not equivalent, to an impure variant evaluated by De la Torre et al. with a composition of $Ca_{2.95}Mg_{0.03}Al_{0.04}Si_{0.98}O_5$.[11] To evaluate such a system, a supercell ($3 \times 1 \times 1$) having 486 atoms was constructed by expanding the unit cell (162 atoms) along the x-coordinate, where two Ca atoms were substituted with two Mg atoms and one Ca and one Si atom were further substituted by two Al atoms, respectively, in the lattice.

In general, the calculations are able to reproduce correctly the lattice parameters, and X-ray signatures for pure TI-Ca_3SiO_5 [see Table 1 and Figure ES2 (Supporting Information)], though less precisely for the impure Ca_3SiO_5 composition.[11,17] From analysis of the structural parameters (Figure ES2b and Table ES1, Supporting Information) it is noted that the calculated and experimental parameters are in reasonable agreement for $2\theta \leq 41°$, after which some deviations are noted. While the reasons for such deviations are multifold, the following are contributing factors: (a) consideration of partial occupancies of atoms in experimental crystal structure refinements, which are not considered in calculations; (b) the construction of the supercell by expanding the unit cell only in the x-coordinate, which may induce directional bias in the structural parameters; and (c) while similar, the composition of the experimental and calculated structures is not equivalent. These aspects would all result in small, but definable, differences between the measured and calculated X-ray patterns.

dx.doi.org/10.1021/cg401647f | Cryst. Growth Des. 2014, 14, 2158−2171

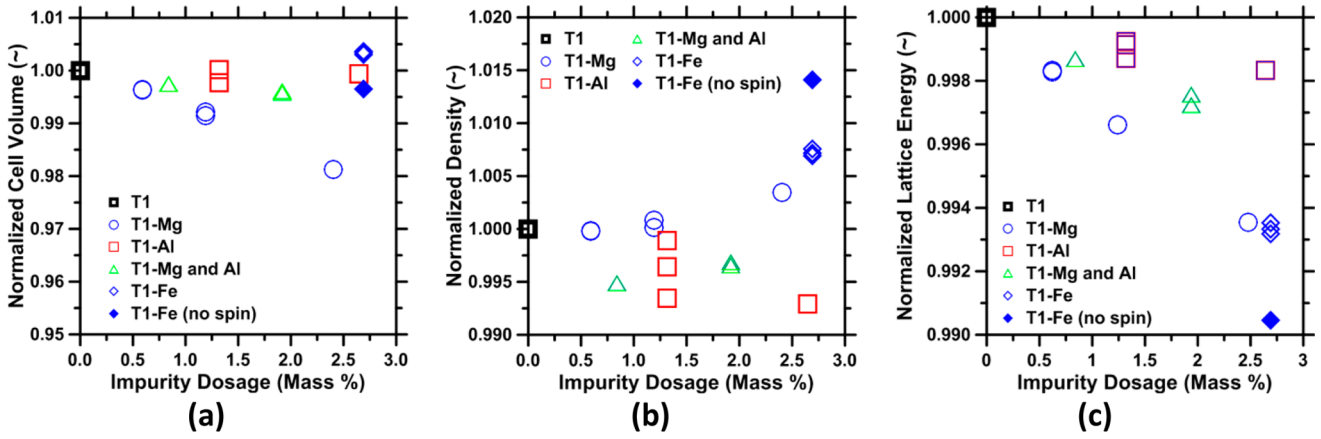

Figure 2. Trends in (a) the normalized cell volume, (b) the normalized density, and (c) the normalized lattice energy as a function of the impurity concentration (dosage).

The calculated enthalpy of formation, though in very good agreement with other computational studies,[28] is underestimated by ≈9% (relative to the constituent elements[29]) and ≈7% (relative to the constituent simple oxides)[30] as compared to experiment. However, given the difficulty in addressing thermodynamic properties at the DFT level and the uncertainty affecting experiments, our results can be considered satisfactory.[31,32] Finally, the elastic constants were determined for the pure and impure TI-Ca_3SiO_5 variants constructed. To the best of the authors' knowledge, the comprehensive set of elastic constants for TI-Ca_3SiO_5 is reported herein for the first time. In fact, comparison with experimental results are currently only available for the Young's modulus of pure TI-Ca_3SiO_5, for which the value of 145.3 GPa reported herein is in good agreement with measurements (E_{EXP} = 135−147 GPa[33]). The only checkpoint available for the impure variant (Figure ES2b, Supporting Information) is for alite (E_{DFT} = 141.7 GPa vs E_{EXP} = 125 GPa[33]), which is in good agreement in spite of differences in the crystal system and the impurity content.

The results of the MAS NMR simulation are shown in Figure ES3 (Supporting Information). For ^{43}Ca NMR, distinct NMR peaks are located in the region from 30 to 130 ppm, being concentrated between 80 and 105 ppm. For pure TI-Ca_3SiO_5, the calculated values of the coupling constant, C_Q ranged between 1.2 and 5.8 MHz, in reasonable agreement with the findings of Moudrakovski et al.[34] On substitution of Al species, e.g., at Si and Ca sites, the ^{43}Ca NMR signal shows some line broadening, which may indicate the initiation of displacive phase transitions toward the T2-T3 and M series of Ca_3SiO_5 polymorphs.[34] In the case of ^{29}Si NMR, discrete resonance peaks located between −68 and −76 ppm are noted (for pure TI-Ca_3SiO_5) corresponding to nine isolated Q^0-$[SiO_4]^{4-}$ tetrahedra, as highlighted by Stephan et al. and Moudrakovski et al.[34,35] Once again, Al substitution results in broadening and some superposition of the NMR signals.[34,35] It is noted that when Al species substitute in proximate Ca and Si sites (i.e., case 7, where Ca−O−[Si] changes to [Al]−O−[Al]), the local organization of tetrahedral units is altered. For example, the new $[AlO_4]^{5-}$ tetrahedra formed connect to each other via a bridging oxygen atom, with the central $[AlO_4]^{5-}$ tetrahedron also being linked to a neighboring $[SiO_4]^{4-}$ tetrahedron via another bridging oxygen atom. As a consequence, when proceeding from left-to-right (see Figure ES3c, Supporting Information), the [Al]−O−[Al]−O−[Si] units display a Q^1−Q^2−Q^1 configuration.[36] These aspects are discussed further later.

Generally, the bulk modulus can be obtained by two distinct methods: the Reuss−Voigt−Hill (RVH) approximation, based on the elastic constants, and the application of an equation of state (EoS), based on a pressure−cell volume relationship.[37] In order to further confirm the validity of the value of the bulk modulus obtained from the elastic constants, calculations of equilibrium cell volumes under different applied pressure were carried out. Figure ES4 (Supporting Information) shows the total energy versus cell volume (E−V) and the cell volume versus applied pressure (V−P) relationships. The smooth trends indicate that no phase transitions occur as a consequence of the applied pressure. The data sets were subsequently fitted using the Birch−Murnaghan EoS,[37] and the bulk modulus was determined to be 97.1 GPa. This value is slightly underestimated (−3%) with respect to the bulk modulus of 100.4 GPa determined from the elastic constants. Nevertheless, a similar difference (3%) between the two methods was also observed in prior treatments of tricalcium aluminate ($Ca_3Al_2O_6$) by Moon et al.[38] These results and their excellent agreement with experiments represent a valuable checkpoint for our DFT calculations, providing a defined point of reference to compare pure and impure variants of TI-Ca_3SiO_5. The reliability of the DFT calculations thus established sets a clear baseline for addressing the influences of incremental impurity insertions on the structural properties and electronic descriptors of TI-Ca_3SiO_5.

3.2. TI-Ca_3SiO_5 Containing Impurities: Structural and Electronic Properties. *3.2.1. Cell Volumes and Cell Parameters.* As a starting point, incremental step-by-step substitutions were carried out to quantify the effects of impurity insertion on the lattice parameters as a function of concentration (dosage). Expectedly, the introduction of impurities alters both linear and angular lattice parameters (and cell volume) in relation to the type/extent of the impurities themselves. The cell volume is chosen as an initial descriptor, since it is a clumped indicator of cell parameters. For example, atomic compensation effects can influence the cell parameters but not the cell volume and vice versa. However, as can be seen from Figure 2a, the normalized cell volume (i.e., normalized with respect to pure TI-Ca_3SiO_5) reduces monotonically upon Mg insertions (∼2%) while it remains essentially unchanged upon Al insertion (Figure 2a). This effect is attributed to the presence of an Al atom (smaller than Ca) at

dx.doi.org/10.1021/cg401647f | Cryst. Growth Des. 2014, 14, 2158−2171

Table 2. Bond Lengths (Å) and Bond Angles (deg) for Different Impurity Substitutions in TI-Ca_3SiO_5[a]

	bond length (Å)					bond angle (deg)					
	r_1	r_2	r_3	r_4		θ_1	θ_2	θ_3	θ_4	θ_5	θ_6
					Ca site						
case 1 *Ca*–*O*–[Si]	2.345	2.345	2.361	2.361	case 1 *Ca*–*O*–[Si]	180.0	100.3	79.7	79.7	100.3	180.0
case 7 *[Al]*–*O*–[Al]	1.767	1.795	1.822	1.841	case 7 *[Al]*–*O*–[Al]	136.7	111.4	107.9	98.3	95.3	101.9
case 8 *Al*–*O*–[Si]	1.821	1.841	1.916	2.008	case 8 *Al*–*O*–[Si]	158.2	107.8	95.2	94.0	84.5	93.1
case 9 *[Al]*–*O*–[Al]	1.795	1.743	1.816	1.883	case 9 *[Al]*–*O*–[Al]	141.1	109.9	96.8	96.5	97.3	114.9
case 13 *Fe*–*O*–[Fe]	1.850	2.034	2.072	2.073	case 13 *Fe*–*O*–[Fe]	108.7	88.6	103.1	162.8	80.2	97.1
case 14 *[Fe]*–*O*–[Fe]	1.887	1.909	1.919	2.020	case 14 *[Fe]*–*O*–[Fe]	110.5	148.2	106.7	93.8	96.9	89.7
case 16 *[Fe]*–*O*–[Si]	1.860	1.891	1.998	2.051	case 16 *[Fe]*–*O*–[Si]	109.3	148.3	107.8	94.0	96.6	89.8
					Si site						
case 1 Ca–*O*–*[Si]*	1.648	1.655	1.658	1.659	case 1 Ca–*O*–*[Si]*	110.8	107.5	108.5	111.1	109.0	109.9
case 7 [Al]–*O*–*[Al]*	1.753	1.755	1.769	1.811	Case 7 [Al]–*O*–*[Al]*	113.9	107.6	107.0	109.6	107.5	111.3
case 13 Fe–*O*–*[Fe]*	1.762	1.768	1.774	1.810	case 13 Fe–*O*–*[Fe]*	118.0	105.1	101.6	111.9	103.5	116.9
case 14 [Fe]–*O*–*[Fe]*	1.847	1.853	1.867	1.896	case 14 [Fe]–*O*–*[Fe]*	114.1	107.0	104.9	110.1	107.3	113.5
case 16 Ca–*O*–*[Fe]*	1.855	1.860	1.864	1.930	case 16 Ca–*O*–*[Fe]*	113.8	107.3	103.7	112.2	105.6	114.4

[a]The italic notation corresponds to the bond lengths or bond angles sampled.

the Ca position; such insertions are counterbalanced by the formation of a larger $[AlO_4]^{5-}$ tetrahedron in lieu of the $[SiO_4]^{4-}$ tetrahedron. On the other hand, the smaller ionic radius of the Mg atom engenders a reduction in the normalized cell volume, as Mg substitutions for Ca species are increased. Significantly, and in agreement with the work of Stephan and Wistuba,[6] while Mg atoms do influence cell dimensions, Al insertions alter cell angles more substantially, enhancing the distortion of the crystalline lattice. Further, when Mg impurities are present (∼0.9%), the cell volume decreases by around 1.3%, in agreement with the observations of De la Torre et al.[11]

In the case of spin-polarized Fe substitutions, a negligible expansion of the cell volume (<0.5%) is reported. When spin polarization is not imposed, a yet smaller reduction (∼0.2%) in the cell volume emerges. On the basis of energetic considerations, the antiferromagnetic (AF) phase is more stable than both the ferromagnetic (FM) (ΔE = 0.2 eV) and the spin-unpolarized phases (ΔE = 3.0 eV). This order of stability is consistent with DFT calculations of hematite (α-Fe_2O_3) by Rollmann et al.,[39] who reported the relative stability of AF systems with respect to the spin-unpolarized phase to be on the order of 0.15 eV/atom. Rollmann et al. also noted that the equilibrium volume of the AF state was larger than that of spin-unpolarized phase, a trend consistent with this work. The reported volume expansion for the Fe system is due to (1) the atomic radius, which is larger for Fe than for Al, and (2) the effects of magnetic coupling between neighboring atoms, which induces a lattice expansion, a behavior similar to that observed in alloys.[40]

Finally, the simultaneous aliovalent substitution of Mg and Al causes a slight reduction of the cell volume (−0.5%), which is similar to the trend noted in the case of only Al substitutions. This result indicates an averaging effect related to the influence of an atomic substituent on its local electronic neighborhood. Overall, the trends in the calculated cell volumes reflect that of the valence-to-ionic radius ratio (Z/r) of the substituent; thus, Al > Fe > Mg when spin polarization is not considered and Fe > Al > Mg when spin polarization is imposed. It should additionally be noted that, for all cases, the change in cell angles is no larger than 0.8°; this indicates that for all the considered substitutions, a crystal system or space group transition is unlikely to occur.

Figure 2b shows the normalized density (i.e., normalized with respect to pure TI-Ca_3SiO_5) of all the Ca_3SiO_5 variants as a function of the impurity concentration. In general, changes in density are small and in the range ≈±2%. It should be noted that, broadly, while the trends in density should be expected to be correlated with the cell volume, this is not always the case. Such an anomaly is related to the fact that the density is influenced by three aspects: (a) the cell volume, (b) atomic weight of the substituent and its concentration, and (c) species that is substituted. For example, in the case of Mg, a reduction in the cell volume results in an increase in density inspite of the substituent species (Mg) being lighter than the substituted (Ca) one. Thus, in this case the reduction in cell volume counterbalances atomic weight effects. However, in the case of Al or Fe impurities where the cell volume remains unchanged (Al) or only slightly increases (Fe), density trends are dictated by atomic weights. Thus, the substitution of an atom lighter than the one it replaces results in a reduction in the density (e.g., Al substitution), while the insertion of heavier species (e.g., Fe atoms) results in larger densities.

Figure 2c shows trends in the normalized lattice energy as a function of the impurity concentration, revealing that the lattice energy becomes less negative with insertion of impurities. This is unsurprising since impurity insertions are (often) expected to destabilize a condensed phase. When the effects of spin polarization are considered, this destabilization, as averaged across the unit cell, ranks as (Figure 2c) Mg ≈ Fe > (Mg + Al) > Al, as indicated by the magnitude of the negative slope, thus suggesting that the average bonding strength inversely decreases from the stronger covalent (i.e., Al and Fe, participatory in tetrahedron formation) to the weaker ionic species (Mg). It should be noted that the response of Fe-bearing phases is complicated by the magnetic spin states imposed. Further, when substitutions are induced at equivalent dosage but at different atomic sites, the lattice energy shows slight change across the Al- and Fe-doped systems but remains essentially unchanged for Mg insertions. This suggests that, at least from a thermodynamic perspective, there is little effect of atomic site(s) and thus site preference on phase stability. While this outcome is unsurprising, in the case of isovalent substitutions, it also remains consistent across single/multielement aliovalent substitutions, which induce local violations of charge neutrality. This suggests that the dominant means of

dx.doi.org/10.1021/cg401647f | Cryst. Growth Des. 2014, 14, 2158−2171

ensuring charge balance is due to a rearrangement of O atoms in the local atomic neighborhood rather than to the valence of the substituent species.

3.2.2. Atomic Rearrangements. Impurity substitutions and their location within the crystal lattice will, generally, tend to alter the equilibrium of the structure. To better understand these aspects, analysis of the rearrangements of silicate, aluminate, and ferrite tetrahedra upon impurity insertion was performed. We note that none of the $[SiO_4]^{4-}$ groups are affected by Mg doping, indicating that the coordination state of the Ca atom/site is unaltered on Mg insertion. In other words, Ca polyhedra experience negligible (if any) deformation, and the Si−O bond lengths remain unchanged when Mg species (results not reported in Table 2) are inserted into the TI-Ca_3SiO_5 lattice (cases 2−6). The substitution of Al into the lattice can occur either with respect to a Si or a Ca site.[4] In the former case, the persistent Al tetrahedron does not display any rotation (i.e., change in angular orientation) or distortion (i.e., change in volume) with respect to its Si counterpart. In contrast, a substantial rearrangement appears when Al occupies a Ca site, that is, when two Al atoms are inserted at proximal Ca and Si sites respectively (case 7). In this case (where Ca−O−[Si] changes to [Al]−O−[Al]), the Al species occupying the Ca position attracts interstitial O atoms to form a new $[AlO_4]^{5-}$ tetrahedron which bonds to the Al tetrahedron (i.e., an Al_{IV} organization[41]) that occupies the (original) Si site via a bridging oxygen atom. This is due to the covalent nature of the Al−O bond, which is stronger than the ionic Ca−O bond. The new $[AlO_4]^{5-}$ tetrahedron formed from the interstitial oxygens shows substantial distortion, as highlighted by an increase in the bond length and deviation of bond angles from the ideal tetrahedron angle of 107.9° (Table 2). It is important to point out that this new Al tetrahedron no longer forms when an Al insertion is relocated to a Ca site separated from the initial Si site (case 8), in which case Al maintains an octahedral organization (i.e., $[AlO_6]^{9-}$, corresponding to Al_{VI}[41]). These two Al-doping scenarios thus explain simultaneous observations of Al_{IV} and Al_{VI} via ^{27}Al NMR in realistic Ca_3SiO_5 systems. As such, it appears that in the case of proximate Al substitutions (i.e., in a colocated Ca and Si site), the need to achieve local charge balance forces the formation of a new $[AlO_4]^{5-}$ tetrahedron, to counterbalance charge and ionic size misfits caused by Coulombic interactions between the Al_{Ca}^{+} and Al_{Si}^{-} sites, respectively. However, when Mg and Al substitutions coexist, their effects on atomic rearrangement appear to be independent, showing that Mg at a Ca site has a negligible impact, but Al insertion at both Si and Ca sites strongly influences the local atomic arrangement, as discussed above. It should also be noted that Q^1-$[SiO_4]^{4-}$ tetrahedra in impure TI-Ca_3SiO_5 does not exhibit distortion as compared to ordinary Q^0-$[SiO_4]^{4-}$ configurations, even when the former Q^1 species is bonded to a $[AlO_4]^{5-}$ tetrahedron. This is likely on account of the higher bond strength of the Si−O bonds, a point which is revisited later.

Similar to Al, the substitution of Fe in the lattice can occur either with respect to Si or Ca sites or atoms. Here, spin polarization plays an important role on atomic arrangements. Unlike Al, in the spin-unpolarized system (case 13, though physically unrealistic) the insertion of a Fe atom at a Si site results in the formation of a $[FeO_4]^{5-}$ tetrahedron (i.e., Fe_{IV} coordination) similar to its $[AlO_4]^{5-}$ counterpart. Further, upon Fe insertion at a proximal Ca site no $[FeO_4]^{5-}$ tetrahedron is formed, with Fe_{VI} coordination being maintained, in contrast to the Al-doping case wherein Al_{IV} coordination is maintained in the case of proximate doping. In contrast, when the AF and FM spin phases (cases 14 and 15) are considered, substantial rearrangements are seen when Fe atoms occupy proximal Ca and Si sites. For example, at the Si site, the $[FeO_4]^{5-}$ tetrahedron is substantially expanded due to magnetic couplings between the different atomic species as compared to closed shell systems. This expansion pushes away the bridging O atoms in the [Fe]−O−[Fe] case (with respect to the original Ca−O−[Si] arrangement), causing these oxygens to bond with the Fe atom substituted at the Ca site. This results in the formation of a new $[FeO_4]^{5-}$ tetrahedron at the Ca site at the expense of the Ca polyhedron; i.e., when [Fe]−O−[Fe] results, Fe_{IV} coordination is maintained at both doping sites. It should be noted that the Fe tetrahedron thus formed is substantially more distorted than the $[AlO_4]^{5-}$ feature (i.e., formed at the Ca site) discussed above. Similar to the Al-doped systems discussed above, Fe-doping results in the formation of the Q^1−Q^2−Q^1 ([Fe]−O−[Fe]−O−[Si]) tetrahedral configurations (see Figure ES3c, Supporting Information) in spin-polarized Fe systems, once again with little if any distortion being noted in the Q^1-$[SiO_4]^{4-}$ tetrahedra compared to Q^0-$[SiO_4]^4$ structures. Thus, it appears as though, when spin polarization is considered and Fe atoms are inserted at proximal Ca and Si sites (i.e., at the bridged Ca−O−[Si] sites), the formation of two $[FeO_4]^{5-}$ tetrahedra ensures charge balance similar to the situation occurring in the case of $[AlO_4]^{5-}$ tetrahedra. Also, for case 16, where the Fe atoms are not adjacent, Fe occupying the Ca site induces the formation of a new $[FeO_4]^{5-}$ tetrahedron (i.e., Fe_{IV} coordination), which occurs due to the strong ionic interactions between Fe and O atoms associated with strong localization of charge density. Contrastingly, such a tetrahedron does not form in the case of nonadjacent Al insertions where Al is substituted at a Ca site (case 8).

4. INFLUENCE OF IMPURITIES ON SUBSTITUTIONAL SITE PREFERENCE AND PHASE STABILITY

In the order implemented herein, Mg^{2+} species can induce a 1:1 substitution at a Ca^{2+} site. On the other hand, two (Al^{3+} or Fe^{3+}) species induce simultaneous substitutions at both Ca^{2+} and Si^{4+} sites, respectively, allowing preservation of charge balance of the unit cell. While this nature of substitutions is expected,[4] it is difficult to resolve the exact position of different substitutional sites, an aspect which especially impacts atomic coordination's in the case of aliovalent doping. To better understand these aspects, the enthalpy of formation of all the different TI-Ca_3SiO_5 polytypes is illustrated in Figure 3. Both the type and nature of substitution (i.e., element and insertion site) impact the formation enthalpy (i.e., with respect to the simple oxides, eq 2), indicating a thermodynamic preference for certain substitution sites at the expense of others without inducing any phase transitions and/or transformations.[11,42] A decrease in the enthalpy of formation, with increasing impurity concentration, suggests that TI-Ca_3SiO_5 becomes more and more unstable with impurity insertion. This is an expected outcome, as defects would increasingly destabilize a condensed phase in relation to their number and density.

A more detailed examination of formation enthalpies corresponding to the same concentration but at different sites suggests that Al/Fe impurities prefer proximity in the lattice, while in contrast, Mg atoms do not show any specific site preference. In the case of codoped (Mg + Al) systems, while

dx.doi.org/10.1021/cg401647f | Cryst. Growth Des. 2014, 14, 2158−2171

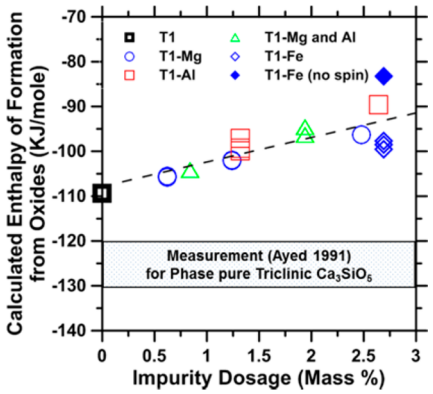

Figure 3. The enthalpy of formation from the elements as a function of the impurity dosage.

the two Al atoms desire proximity to each other, the Mg and Al species desire to be separated from each other (i.e., demonstrating interimpurity exclusivity). This outcome is related to the above discussion wherein, when in proximity (i.e., in the case of substitutions at proximate Ca and Si sites) Al or Fe species induce the formation of new Al or Fe tetrahedra at the Ca site. This is also consistent with the rearrangement of the charge density distributions at the cation (Ca) sites and surrounding oxygen (O) atoms. This latter response, which is noted in the event of aliovalent substitutions, occurs as the impurity species attract each other due to Coulombic interactions (i.e., between Al_{Ca}^{+} and Al_{Si}^{-} or Fe_{Ca}^{+} and Fe_{Si}^{-} species). Thus, the distance between substitution sites is a relevant parameter that describes the "favorability" of aliovalent insertions. Furthermore, it is noted that spin-unpolarized atomic species induce a higher extent of lattice destabilization (i.e., for Fe, less negative enthalpy). However, given the unphysical nature of this case, it would not be appropriate to read further into this aspect. It should be noted that, in general, while there exists a numerical difference in the enthalpy values for substitutions carried out at similar concentration but different sites, this distinction cannot be considered as absolute. In fact, in addition to classical thermodynamic considerations discussed herein, kinetic features, i.e., of ion diffusion in the melt phase and within a crystalline lattice, which are not considered in this work, would also be expected to influence considerations of phase transition(s) and atomic site preference as the transport of species occurs in the melt.[4] As such, while it is clear that phase stability is compromised by the impurity type and insertion site, further work is yet needed to more precisely resolve aspects of substitutional site preference in the silicate lattice.

5. INFLUENCE OF IMPURITIES ON THE MECHANICAL PROPERTIES

A systematic study was conducted to determine changes induced in the mechanical properties of TI-Ca_3SiO_5 with respect to different impurity substitutions. The moduli of all the different cases considered, calculated using the RVH approximation, are reported in Table 3, with the results for pure TI-Ca_3SiO_5.[23] The calculated values for pure TI-Ca_3SiO_5 are in very good agreement with experimental results.[33] Furthermore, Table ES3 (Supporting Information) lists the complete set of derived directional elastic constants (in GPa) relevant to pure and impure triclinic Ca_3SiO_5. The mechanical stability of the material is ensured within the Born criterion[43] that restricts the overall C_{ij} matrix, ensuring that its principal minor determinants are positive. This analysis also confirms that the systems considered herein are mechanically stable. In general, and similar to alite, the elastic (i.e., Young's) and shear moduli decrease when impurities are present, with Al (∼5%) and Fe (∼6%) showing a more substantial influence than Mg impurities (Figure 4a,b). This trend in the mechanical properties is closely replicated by the diagonal components of the stiffness tensor, (a) C_{11}, C_{22}, C_{33} and (b) C_{44}, C_{55}, C_{66}, which encompasses the longitudinal and shear components, respectively. Furthermore, independent of the type/extent of doping, the degree of longitudinal (C_{33}/C_{11} = 1.038 ± 0.018) and shear (C_{66}/C_{44} = 0.743 ± 0.009) anisotropies is similar across all cases. Analogous to other systems, it is noted that impurities destabilize the structure, thus decreasing its stiffness. When Fe impurities are present, magnetic coupling/spin induce reductions in the mechanical moduli, an effect similar to that reported in intermetallic compounds and which occurs due to magnetic influences on the electronic structure.[40] Finally, it is also interesting to note that the trends for both elastic and shear moduli are reasonably correlated with the cell volume (Figure 4c), indicating that the local influences of impurities on atomic bonding and structural expansion/contraction result in very direct alterations of the stiffness (and thus mechanical stability) of the polymorph considered.

6. INFLUENCE OF IMPURITIES ON ELECTRONIC DESCRIPTORS

6.1. Tetrahedron Distortion. The effects of impurity species on the electronic structure of both pure and impure variants of TI-Ca_3SiO_5 are investigated. To characterize changes in the nature of chemical bonds and to describe differences arising across dopant neighborhoods, the 3D charge density difference of pure TI-Ca_3SiO_5 with and without impurity ions was obtained (Figure 5). More specifically, the 3D charge density differences were determined by subtracting the charge density of the isolated atoms from the total charge density of the overall cell. It is first noted that when Mg atoms substitute Ca species, the charge density difference isosurface remains unchanged, indicating little if any change in electronic

Table 3. Mechanical Moduli (GPa) of Pure and Impure TI-Ca_3SiO_5 Phases

	case 1	case 2	case 4	case 5	case 6	case 7	case 10	case 11	case 13	case 14
K	100.35	100.47	100.89	100.27	100.90	98.71	97.13	98.60	100.87	97.85
G	57.72	57.61	57.41	57.03	57.86	56.13	54.89	55.97	55.62	54.15
E	145.31	145.09	144.76	143.82	145.73	141.57	138.57	141.20	140.96	137.16
v	0.26	0.26	0.26	0.26	0.26	0.26	0.26	0.26	0.27	0.27
M	155.73	155.55	155.33	154.33	156.23	151.91	148.80	151.55	151.79	147.63

dx.doi.org/10.1021/cg401647f | Cryst. Growth Des. 2014, 14, 2158−2171

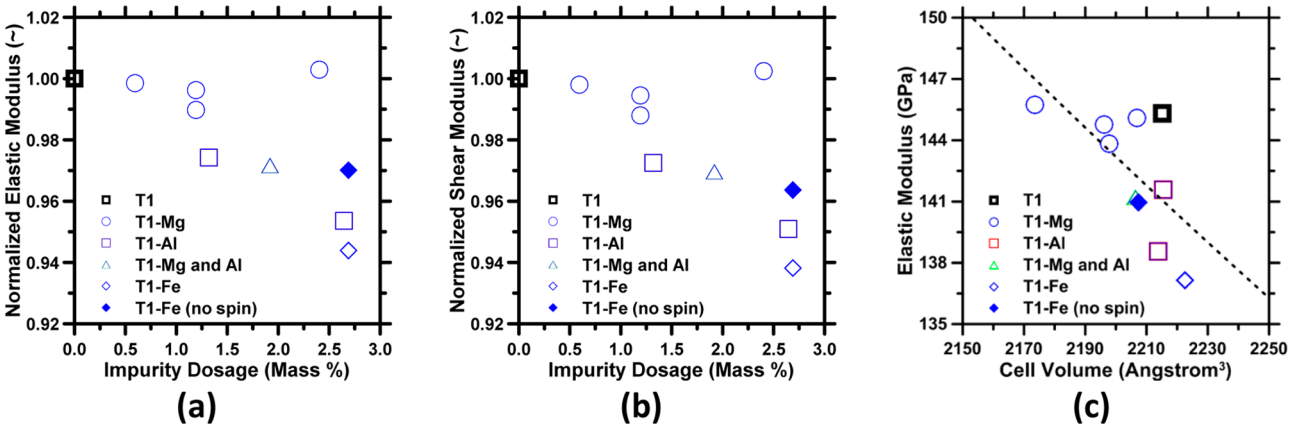

Figure 4. (a) The normalized elastic modulus and (b) the normalized shear modulus as a function of the impurity dosage and (c) the elastic moduli as a function of the cell volume.

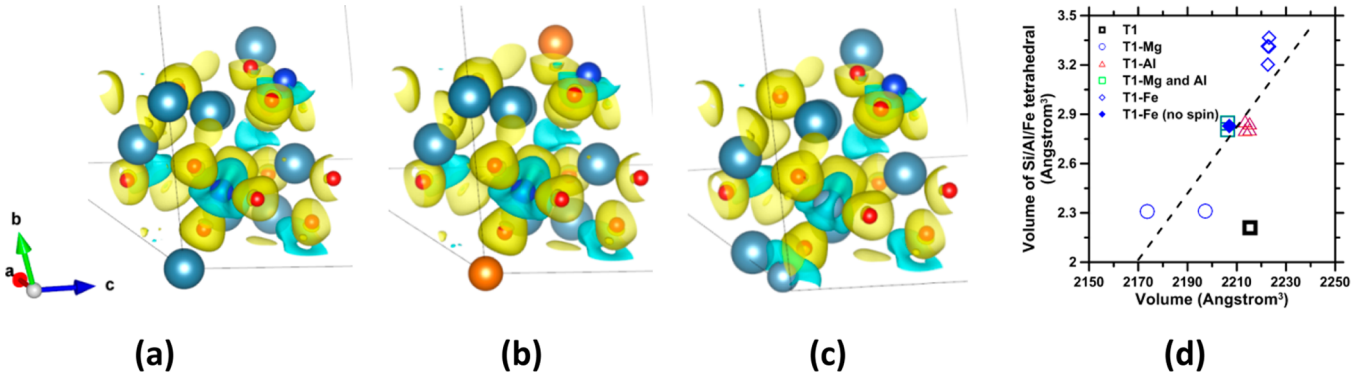

Figure 5. Charge density difference of (a) case 1, TI-C_3S; (b) case 4, TI-C_3S with Mg impurities; and (c) case 7, TI-C_3S with Al impurities. The isosurface level is set at 0.008 $e^-/Å^3$, wherein yellow and blue shades correspond to positive and negative charge densities, respectively. Calcium (Ca), silicon (Si), magnesium (Mg), aluminum (Al) and oxygen atoms (O) are represented as gray, blue, orange, small gray and red spheres, respectively. (d) The volumes of Si/Al/Fe tetrahedra as a function of the corresponding unit cell volumes.

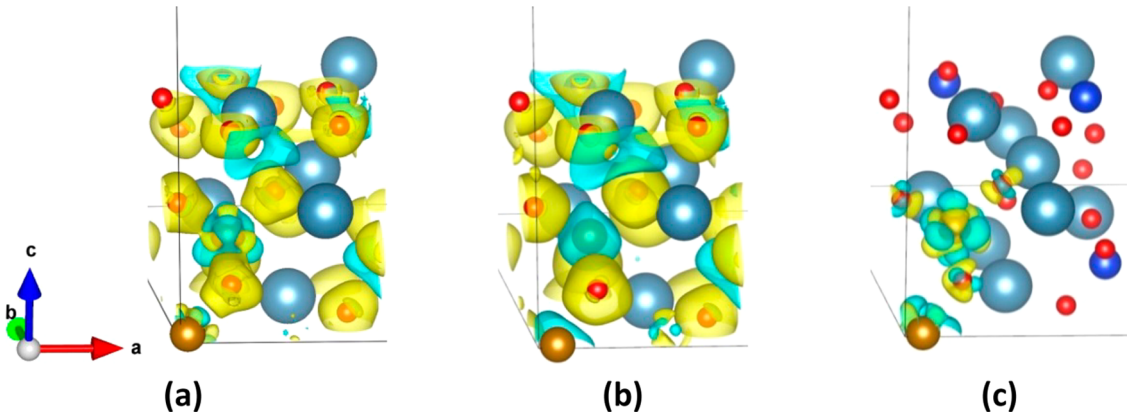

Figure 6. Charge density difference of Fe: (a) case 13, no spin; (b) case 14, AF spin; (c) between AF spin and nonspin. The isosurface level is set at 0.01 $e^-/Å^3$, wherein yellow and blue colors correspond to positive and negative charge densities. Calcium (Ca), silicon (Si), iron (Fe), and oxygen atoms (O) are represented as gray, blue, brown, and red spheres, respectively.

configuration (Figure 5a,b). On the other hand, electronic differences are appreciable when Al substitutes at Ca sites, as shown in Figure 5c. The charge density around Si or Al substituted at the Si site shows a tetrahedron-like geometry, though the orientation differs with respect to that of a perfect tetrahedron. This anisotropic distribution of the charge density indicates the covalent nature of O atoms bonded to Si or Al. The charge density rearranges to produce a tetrahedron-like distribution when Al is substituted at the Ca site. The charge density at the bottom of the new tetrahedron facing the bridging O atom (for Al insertion at Ca sites) resembles the situation occurring when Al atoms are inserted at the Si site. Here, the bridging O atom creates a channel for charge transfer between the two interlinked $[AlO_4]^{5-}$ tetrahedra. As discussed above (case 7), the necessity to achieve (local) charge balance forces the formation of a "new $[AlO_4]^{5-}$ tetrahedron" at the Ca

dx.doi.org/10.1021/cg401647f | Cryst. Growth Des. 2014, 14, 2158−2171

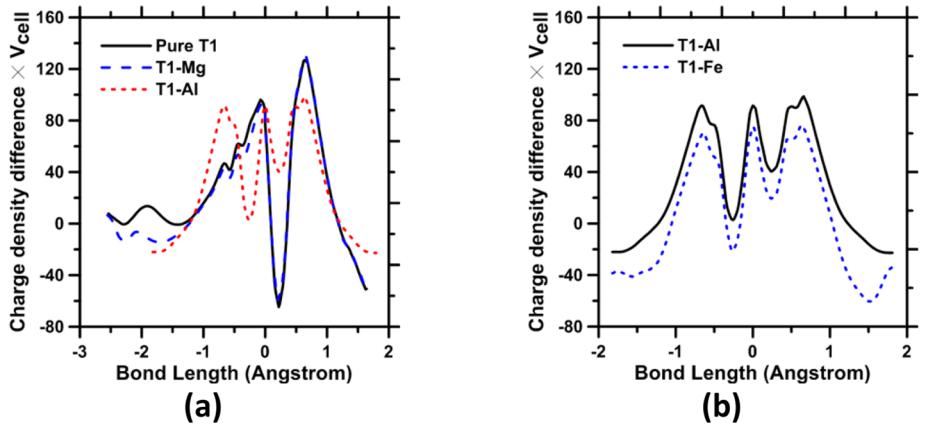

Figure 7. The charge density difference × V_{cell} (e) as a function of the bond length. The 0 point coincides with the bridging O atom, negative values correspond to Ca or substitutions at the Ca site, and positive values correspond to Si or substitutions at the Si site. (a) pure TI-Ca_3SiO_5 and TI with Al/Mg substitutions. (b) TI-Ca_3SiO_5 with Al and Fe substitutions.

site. The need for charge balance also induces expansions of the $[AlO_4]^{5-}$ tetrahedron at both Si and Ca sites. Figure 5d shows the volumes of the Si/Al/Fe tetrahedra as a function of cell volumes. Such investigations reveal a linear relationship between the volumes of the local tetrahedra and the cell volume of the system. Furthermore, while Mg substitutions only slightly increase the $[SiO_4]^{4-}$ tetrahedral volumes, Al substitutions induce ≈30% expansion with respect to pure T1-C_3S. In the event that both Mg and Al species are substituted, the latter plays a dominant role in modification of the tetrahedral volumes wherein extended $[AlO_4]^{5-}$ tetrahedra connect to each other through the "bridging" O atom. The tetrahedron-like negative charge density around Al has a smaller volume than that of pure and Mg-substituted Ca_3SiO_5, which seems to indicate that when an Al atom is substituted at the Si site, less charge transfer occurs via the O atoms, but charge balance is restored by the formation of a tetrahedron-like charge density at the substituting Ca site.

When Fe atoms are substituted, spin polarization has a dramatic impact on the charge density difference. For comparison, the spin-unpolarized phase is also reported and commented on. This case, although unphysical, shows a directional and delocalized charge density distribution. This situation drastically changes when spin polarization is considered, and the system shows a much more isotropic and localized (i.e., spherical) charge distribution. This response seems to imply that spin polarization strengthens charge localization and balances the electronic charge density. Concurrently, the charge density distribution changes from an anisotropic to a more isotropic form, weakening the strength of covalent bonds. This detail provides an explanation for the decrease of the elastic moduli when spin-unpolarized Fe atoms are substituted into TI-Ca_3SiO_5 (Figure 4). In order to investigate the effects of spin polarization, the charge density difference map between spin-polarized and spin-unpolarized states is reported in Figure 6c. As expected, typical 3d orbital characteristics related to the presence of Fe atoms near O sites appear, suggesting that the d-orbitals of the Fe atoms strongly hybridize the p orbitals of the O atom, leading to a complete localization of charge around the Fe atoms. This aspect contributes to the $[FeO_4]^{5-}$ expansion associated with the AF configuration. In relation to changes in the tetrahedra, the spin-unpolarized system induces an expansion comparable to that induced by Al insertion. On the other hand, both AF and FM solutions show an expansion 50% larger than the pristine lattice (see Figure 5d). In Figure 6b, a larger expansion corresponds to a smaller charge density around Fe atoms; this also suggests relatively less charge transfer from Fe to O atoms. As such, magnetism plays an important role in regard to both the volume expansion and the (re)distribution of charge, which influences the mechanical properties. It has been reported that in Ni-rich B_2−NiAl intermetallic compounds, in contrast to the presence of closed shell atoms, Fe impurities can result in substantial dilation and softening effects.[40] Such a trend appears to be consistent with the results reported here, where elastic moduli decrease when Fe is substituted and AF and FM solutions are imposed (Figure 4).

To further probe the bonding characteristics of the various species, we look into changes in the electronic charge density normalized with respect to the bond length along a path surrounding the defects (e.g., Ca−O−[Si], Mg(Ca)−O−[Si] ,or Ca(Al)−O−Si[Al]), where the parenthetical identifier "[X]" indicates the X dopant atom occupying a given atomic position in TI-Ca_3SiO_5. Once again, Mg and Al substitutions show substantial contrast. In Figure 7a, the oscillating response of the charge density difference normalized with respect to the corresponding bond length displayed by pure TI-C_3S is replicated by the Mg-doped phase for which a small perturbation is noted beyond −1.5 Å, corresponding to the Mg−O bond (to the left). In general, wide oscillations (i.e., corresponding to the absolute area under the curve) correspond to stronger bonding. Thus, in TI-Ca_3SiO_5 the Ca−O bond is weaker than its Si−O counterpart, with such differences arising from the ionic nature of the former and covalent nature of the latter. Mg substitutions at Ca sites do not change the charge density profile. However, when Al atoms are inserted (e.g., at adjacent Ca and Si sites), the charge profile changes drastically. Thus, while O−Al(Si) bonds are weakened, a new chemical bond is formed at the Al(Ca)−O position. This is consistent with the formation of a new $[AlO_4]^{5-}$ tetrahedron, as previously discussed. This rearrangement also indicates charge transfer from Al(Ca)−O to O−Al(Si), an additional factor which allows for this system to achieve local charge balance. The bonding behavior of Al substitutions at both the Ca and Al sites is similar, indicating a *symmetric response* with respect to both substitution sites. In the case of the AF-Fe system, the charge density response resembles that noted in the case of Al doping, despite a slight negative shift. This is related

dx.doi.org/10.1021/cg401647f | *Cryst. Growth Des.* 2014, 14, 2158−2171

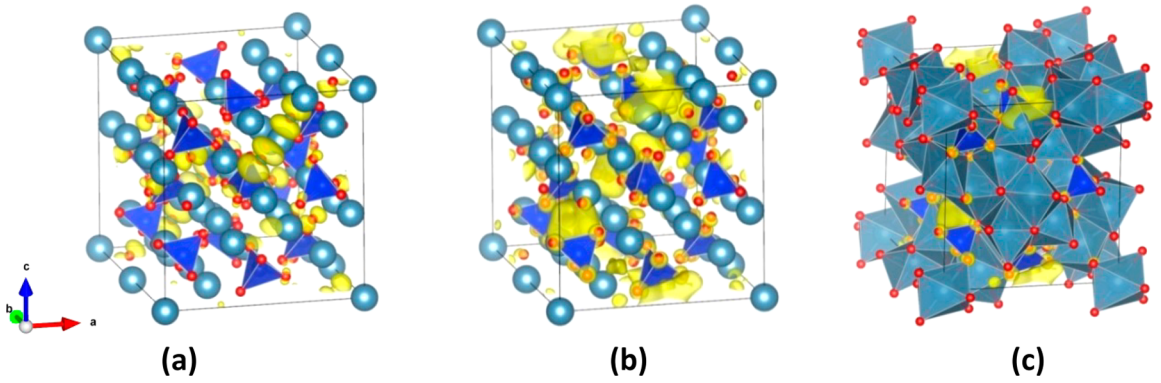

Figure 8. Partial charge density for pure TI-Ca_3SiO_5 of (a) the VBM, (b) the CBM, and (c) the CBM remarked with polyhedra. Calcium (Ca), silicon (Si), and oxygen atoms (O) are represented as gray, blue, and red spheres, respectively.

to the "covalency character" of the involved atomic species, showing the Fe−O−Fe bonds to be the least covalent with respect to those that involve Al and Si (i.e., with Si being the most covalent in nature). Further, the reported charge density distribution is consistent with the formation of a new tetrahedron centered on Fe (as also noted for Al) and a balance of charge ensured by charge transfer from the Si to the Ca site.

6.2. Charge Transfer. Charge transfer plays an important role in describing structural rearrangement and chemical reactivity. Different schemes have been proposed to analyze local partial charges on atoms, such as Bader charge and Lowdin population analysis.[44−46] Bader charge analysis suggests that the presence of the Mg atoms decreases the overall charge of the system (−0.10e). On the contrary, the two Al atoms donate 5.26e instead of 5.43e (donated by the Ca + Si species), and thus, the charge transferred to the system is reduced by 0.17e. Furthermore, Bader analysis shows that the AF system donates 3.08e, thus reducing the charge transferred to the system by 2.35e. Such differences, besides causing charge localization, make TI-Ca_3SiO_5 containing Al and Fe impurities more susceptible to electrophilic attack.

Chemical reactivity, which in molecules can be related to the highest occupied molecular orbital (HOMO) and lowest unoccupied molecular orbital (LUMO) characteristics, can in bulk systems be described by the valence band maximum (VBM) and the conduction band minimum (CBM). While the VBM describes electrophilic attack, CBM governs nucleophilic attack. Figure 8 shows the partial charge density at the VBM and the CBM of TI-Ca_3SiO_5. These findings are consistent with those of Durgun et al.,[16] who reported similar features for MIII-Ca_3SiO_5. Interestingly, the partial charge density at the CBM only exists at interstitial sites between the Si tetrahedra and Ca polyhedra, suggesting that the interstitial sites would experience nucleophilic attack before the $[SiO_4]^{4-}$ tetrahedra and/or Ca polyhedra, respectively. Further, the influence of impurity species on partial charge densities at the CBM and VBM is resolved (Figure ES6, Supporting Information). While Mg impurities do not modify the VBM, Al species induce a slight change on the order of 0.001 e/Å^3. In the case of CBM, charge density for the central Mg atom decreases, but that of the corner Mg increases. Interestingly, Al species also cause a decrease in the charge density at the center of the cell where Al is not substituted; this induces a degree of localization around the Ca site due to the formation of the new $[AlO_4]^{5-}$ tetrahedron. These results imply that Mg and Al impurities do not broadly modify the reactivity of TI-C_3S under electrophilic attack. Furthermore, both of these impurities (i.e., Mg, Al) have limited influence on the reactivity under nucleophilic attack.[6] This may suggest that unless the insertion of (Mg, Al) species induces the formation of structural imperfections (i.e., dislocations, fractures, etc.), assuming structural similarity, the intrinsic reactivity (e.g., surface reaction rate or the first dissolution rate[47]) of TI-Ca_3SiO_5 with water would not substantially differ between its Mg- and Al-doped variants, a result which is in agreement with experimental evaluations.[6,48] In contrast, a strong charge localization in both VBM and CBM appears when Fe impurities are inserted into TI-Ca_3SiO_5. However, this feature is different when either the AF or the spin-unpolarized Fe systems are considered. In fact, while the partial charge densities of the AF case reveal the T_{2g} and E_g characters of VBM and CBM, respectively, those of the spin-unpolarized case look alike and no appreciable differences are observed. Therefore, it can be concluded that when Fe species are present, reactivity under both electrophilic/nucleophilic attack is highly localized. As such, it can be expected that the decrease in the number/density of reaction sites will be expressed as a substantial decrease in reactivity of TI-Ca_3SiO_5 with Fe substitutions, a conclusion that is in broad agreement with experimental observations.[6] However, it is important to mention two possible interpretations that refer to the appearance of flat bands in the band structure of the Fe-substituted Ca_3SiO_5. In fact, if such flat bands are interpreted as referring to *defect states*, the overall value (and the nature) of the Fe-doped material's band gap remains similar to that of phase-pure TI-Ca_3SiO_5. On the other hand, if a more fundamental physical meaning is assigned to the flat bands, then the value of the band gap would drastically reduce, ranging from that of pure Ca_3SiO_5 to that of Fe-doped Ca_3SiO_5 (see Table 4), leading to an apparent contradiction between the thermochemical indicators and mechanical properties and the

Table 4. Calculated Band Gap of Pure and Impure TI-Ca_3SiO_5

polytype	band gap (eV)
TI (case 1)	3.79
Mg2 (case 4)	3.80
Al2 (case 7)	3.79
Fe-spin unpolarized (case 13)	0.42
Fe2-spin polarized (AF) (case 14)	0.91 (spin-up), 2.17 (spin-down)
Fe2-spin polarized (FM) (case 15)	2.95 (spin-up), 1.55 (spin-down)

dx.doi.org/10.1021/cg401647f | *Cryst. Growth Des.* 2014, 14, 2158−2171

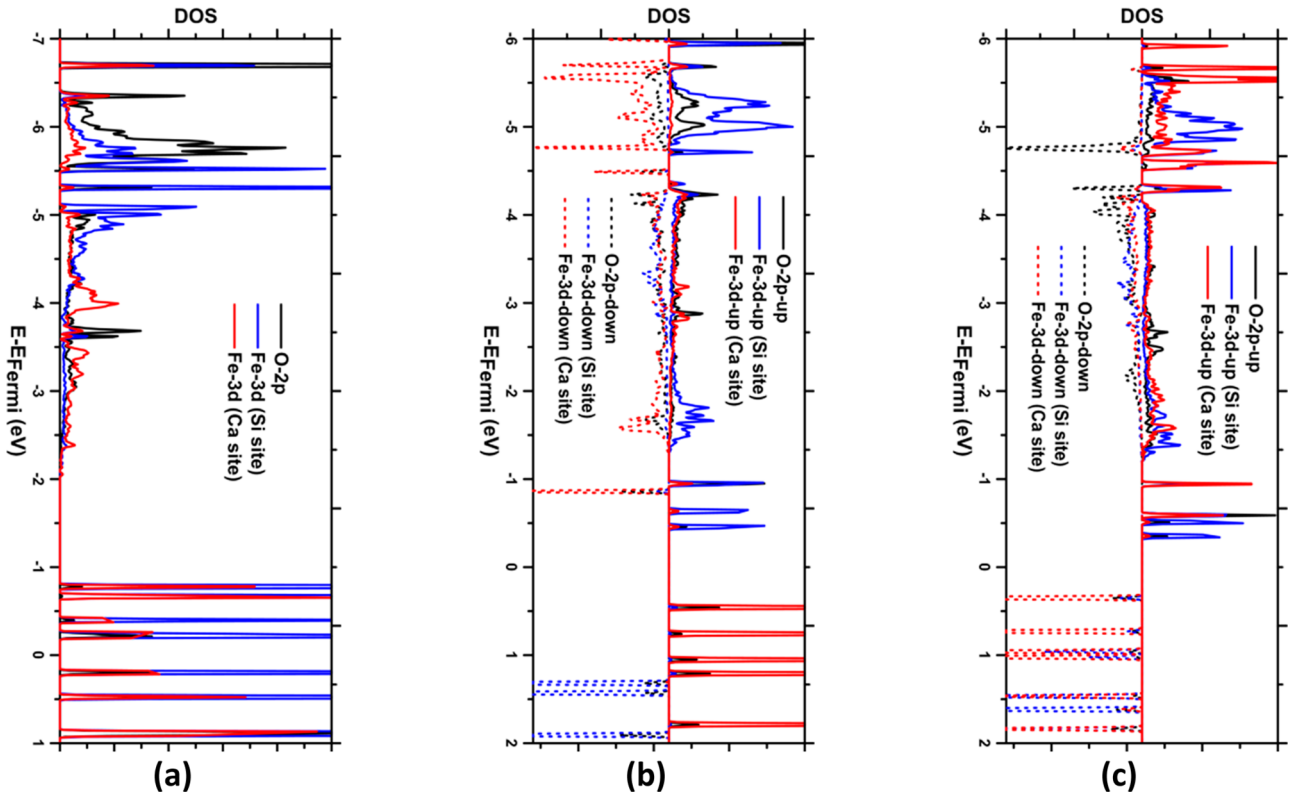

Figure 9. Projected density of state (PDOS) of the 2p orbital of bridging O atoms and Fe atoms at both Si and Ca sites: (a) case 13 (no spin), (b) case 14 (AF), and (c) case 15 (FM).

electronic behavior of the material in describing phase stability and, thus, reactivity alterations as induced by impurity doping.

It should also be noted that, since the cell volumes of the pure and impure systems considered are nominally similar, the maximum isosurface value (MIV, e/Å^3) can be linked to the degree of charge localization.[16] As noted in Table ES4 (Supporting Information), Mg/Al impurities slightly decrease localization at VBM while at the same time they slightly increase charge localization at CBM. On the other hand, when Fe impurities are present, the MIV is about 3 times larger than that of pure TI-Ca_3SiO_5, and strong localization is displayed. In particular, the MIV value increases by 2 orders of magnitude at CBM. However, correlating charge localizations to phase reactivity as inferred from first-principles calculations is difficult and somewhat speculative, since kinetic reactions (e.g., OPC hydration) that are mediated by both the solute and solvent cannot be treated at first-principles levels. Furthermore, since the solvent chemistry has substantial implications on the kinetics of the reactions and on how reaction rates would evolve, these aspects are even harder to interpret.[47] Finally, since the nature of the surface (e.g., in the form/distribution of defects, substitutional or structural) where hydration reactions occur is an important aspect not considered herein, further work is needed to treat these aspects.

In order to investigate the influence of impurities on band gaps, the band structures of pure and impure TI-Ca_3SiO_5 variants are reported in Figure ES7 (Supporting Information). TI-Ca_3SiO_5 shows a direct band gap (3.79 eV) at the gamma point. The insertion of Mg and Al impurities has little impact on the band structure, and this is reflected by the values for the band gaps that remain essentially unchanged as compared to those of pure TI-Ca_3SiO_5 (Table 4). However, while Mg species shift the bands up, Al doping shows the opposite trend. An apparent dramatic decrease in the band gap is reported when Fe impurities are present in the lattice, as characterized by the appearance of very flat bands (see Figure ES8, Supporting Information). Such *dispersionless* behavior has also been observed in other cementing phases, e.g., mayenite ($Ca_{12}Al_{14}O_{33}$), where they have been related to *defect states*.[49] Nevertheless, it is interesting to address the nature of the atomic orbitals related to such states by analysis of the density of states (DOS). Descriptions of the DOS can provide information about the nature of the chemical bonds that, in the cases described herein, appear to show very strong localization emergent from specific atomic orbitals. As such, in specific cases, if it is estimated that wider band gaps correspond to more stable systems, the results suggest that Fe impurities tend to decrease the stability of TI-Ca_3SiO_5.

For the spin-unpolarized system (Figure ES8a, Supporting Information), the five bands below and the five above the Fermi energy correspond to the 10 3d orbitals of the two Fe atoms. The DOS for Fe at the Ca site move toward higher energy levels with respect to the DOS corresponding to Fe atoms substituted at Si sites; this indicates that Fe atoms are more stable in tetrahedral coordination in the lattice. For Fe at the Ca site, the T_{2g} d_{zy} orbitals are occupied at both the VBM and CBM; such a situation is not replicated either when Fe occupies the Si site or in the case of spin-polarized Fe substitutions, for which the orbitals corresponding to T_{2g} and E_g symmetry are filled at the VBM and CBM, respectively. In the AF system (see Figures ES8b,c, Supporting Information), the band gap is governed by the spin-up electrons of Fe atoms at the Ca site (conduction bands) and those of the Fe atoms at the Si site (valence bands). In particular, the CBM corresponds to a d_{z^2}

dx.doi.org/10.1021/cg401647f | *Cryst. Growth Des.* 2014, 14, 2158−2171

electron (red line) and the VBM is dominated by a d_{zx} orbital (green line). These results are visualized in Figure ES6d,h (Supporting Information), where T_{2g} and E_g show significantly different charge distributions. In the FM system, spin-up electrons contribute to the valence bands, while spin-down electrons determine the nature of the conduction bands. In particular, the d_{zx} orbital (green line) and the d_{z^2} orbital (red line) correspond to the VBM and CBM, respectively. The DOS seem to indicate that Fe at the Ca site is stabilized by the spin-up electrons while Fe at the Si site is stabilized by spin-down states.

The PDOS of Fe atoms at the Ca site (for the spin-unpolarized case), by contrast, shows weaker bonding behavior with respect to the neighboring atoms. This result reflects the fact that no new Fe tetrahedron forms when Fe is substituted at the Ca site. For the spin-active Fe-doped TI-Ca_3SiO_5 system, both antiferromagnetic (AF) and ferromagnetic (FM) states (Figure ES8b−e, Supporting Information) are investigated. These results indicate that the d orbitals for the spin-polarized solutions are degenerate. A closer view of DOS near the Fermi energy reveals that VBM is mainly composed of T_{2g} d_{zx} orbitals, while the CBM is determined by E_g d_{z^2} orbitals. This result is consistent with the previous discussion about the nature of the partial charge density at the VBM and CBM. Given the high-spin configuration imposed, the PDOS corresponding to spin-up electrons is completely asymmetric with respect to the spin-down states; this indicates that Fe atoms at both Si and Ca sites show a strong magnetic behavior. For both AF and FM cases, the PDOS of Fe at the Si site is very similar to that of Fe at the Ca site, suggesting that their nature of bonding is similar. As described previously, Fe substitutions at Ca sites induce the formation of a Fe tetrahedron similar to the Fe tetrahedron that forms in the case of substitutions at the Si site. As per crystal field theory,[50] the d orbitals of the octahedrally coordinated atom will tend to split into lower T_{2g} and higher E_g orbitals, in contrast to a tetrahedral coordinated atom, where the splitting is reversed. For Fe atoms substituted at the Ca site, the spin-unpolarized Fe atom cannot induce the formation of new $[FeO_4]^{5-}$ tetrahedron, preserving the octahedral atomic arrangement. Further, for energetic reasons, the transformation from octahedral to tetrahedral coordination increases the stability of the system (Figure ES8, Supporting Information); as such, and in line with the observations above, impositions of spin polarization stabilize Fe-doped systems, as compared to no-spin solutions.

The O 2p PDOS at the "bridging" site (Figure 9) was further analyzed, showing that the O in the AF species has more *softening* in its electronic distribution in comparison with that of the O in the spin-unpolarized Fe system that presents stronger localization. A comparison between the PDOS of Fe 3d and O 2p orbitals also suggests that the Fe d orbitals strongly hybridize with O p orbitals in all three cases (i.e., spin unpolarized, FM, AF). Since the hybridized Fe 3d and O 2p orbitals occupy both the VBM and CBM, this is indicative of [Fe]−O−[Fe] bonding, which is reflected in the geometry of the $[FeO_4]^{5-}$ tetrahedron.[51] The specific geometrical arrangement (and the differences therein) in turn explains why there exist substantial differences in the band gaps of spin-polarized and spin-unpolarized Fe-doped TI-C_3S.

In Figure 9b,c, an interesting difference is noted for the "bridging" O atoms. In the AF system the electronic behavior of the spin states (up and down) is almost identical, indicating that no magnetism can be induced at this O site. By contrast, the DOS of O in the FM system (Figure 9c) clearly shows asymmetric behavior, which suggests induced magnetism at this bridging O atom. To illustrate these results, the magnetic moments of the O atoms nearest to two Fe atom impurities are summarized in Table ES5 (Supporting Information). In the overall system, only nine atoms (i.e., two Fe and seven O atoms) reveal substantial magnetic moments. For these atoms, two $[FeO_4]^{5-}$ tetrahedra with a "bridging" O atom are formed. Furthermore, the magnetic moments in the FM system are larger than those for the AF case, where two of the seven O atoms show dramatic differences. In particular, O1, which is the bridging atom, shows negligible magnetic moment in the AF case as compared to the larger magnetic moment displayed among other O atoms in the FM system. The second of such oxygen atoms is marked "O7" and shows the longest bonding length with the Fe atom accompanied by a remarkably small magnetic moment. The other O atoms having [Fe]−O bonds maintain otherwise similar DOS distributions (Figure 9c).

7. SUMMARY AND CONCLUSIONS

Starting from pure tricalcium silicate (TI-Ca_3SiO_5), first-principles calculations are for the first time employed to investigate the structural, mechanical, and electronic descriptors of this OPC relevant phase. The calculations are validated against experimental values of structural and mechanical properties and thermochemical data for pure and impure TI-Ca_3SiO_5 variants. A comprehensive tabulation of the elastic constants for TI-Ca_3SiO_5 and its variants is reported. In general, substantial sensitivity to the type, nature, and concentration of impurity substitution is noted, revealing spin polarization to be a dominant factor. All impurities are noted to destabilize the crystalline lattice, an observation that reflects across depressions of the thermochemical, mechanical, and electronic properties. While preferences for atomic site substitutions are elucidated, further work is needed to more completely establish site preference aspects in the light of kinetic considerations, being relevant during phase formation in a cement kiln. However, the evidence does suggest that isovalent impurities are broadly insensitive to the substitution site, while aliovalent impurities prefer to substitute in proximity to each other.

New analysis of charge localization and transfer suggests that, in the absence of any structural defects, TI-Ca_3SiO_5 with Mg and/or Al impurities is likely to show an intrinsic reactivity similar to that of pure TI-Ca_3SiO_5. On the other hand, the insertion of spin-polarized Fe impurities is expected to result in depressed reactivity. While worthy of further validation (e.g., see Kumar et al.[47]), the conclusions drawn from DFT-level studies are in agreement with experimental observations. The outcomes of such work are relevant, as starting from a fully *crystallographically consistent template of TI-Ca_3SiO_5*; the research provides guidance regarding how specific manipulations of impurity distributions (and thus crystalline lattices) could be applied to enhance the reactivity of or reduce the energetic processing burden of OPC. In the light of ever increasing environmental pressures bracketing the construction industry, studies of this nature are critical to improve the performance of OPC as a construction material and bring new efficiencies and sustainability to its use. Further work is now in progress to study the interactions between water molecules and specific surfaces of TI-Ca_3SiO_5 to investigate the role of surface structure and defects as direct indicators of cement reactivity.

■ ASSOCIATED CONTENT

Supporting Information

Crystal structures of TI-Ca_3SiO_5 containing impurities, comparisons of simulated and experimental X-ray patterns, calculated parameters for variants of TI-Ca_3SiO_5 containing (Al, Fe, Mg) species, total energy (Ry) versus the normalized equilibrium cell volume, illustration of bond lengths and bond angles, complete directional stiffness constants (in GPa) for pure and impure TI-Ca_3SiO_5, maximum isosurface value (MIV, e/Å^3) for pure and impure TI-Ca_3SiO_5, partial charge density of the VBM and CBM of impure TI-Ca_3SiO_5, band structures of pure and impure TI-Ca_3SiO_5, projected density of state (PDOS) of the Fe 3d orbital in TI-Ca_3SiO_5 containing Fe impurities, and magnetic moments (μB) of Fe and O atoms in the Fe-doped TI-Ca_3SiO_5 system. This material is available free of charge via the Internet at http://pubs.acs.org.

■ AUTHOR INFORMATION

Corresponding Author

*Phone: (310) 206-3084. Fax: (310) 206-2222. E-mail: gsant@ucla.edu.

Notes

The authors declare no competing financial interest.

■ ACKNOWLEDGMENTS

The authors acknowledge full financial support for this research provisioned by the University of California, Los Angeles (UCLA) and National Science Foundation (CAREER Award #1253269). Access to computational resources was provisioned by (a) the Laboratory for the Chemistry of Construction Materials (LC^2), (b) the Institute for Digital Research and Education (IDRE) at UCLA, and (c) the Extreme Science and Engineering Discovery Environment (XSEDE) supported by the National Science Foundation (OCI-1053575 and DMR-130039). The authors acknowledge the support of these resources in making this research possible. The contents of this paper reflect the views of the authors, who are responsible for the accuracy of the data sets presented and do not reflect the views and/or policies of the funding agencies, nor do the contents constitute a specification, standard, or regulation. The authors would also like to gratefully acknowledge Prof. A. G. De la Torre (Universidad de Málaga) for provision of the X-ray diffraction patterns of pure and impure variants of TI-Ca_3SiO_5 shown in Figure ES2 (Supporting Information).

■ REFERENCES

(1) Mercier, J. P.; Zambelli, G.; Kurz, W. *Introduction to Materials Science*; Elsevier Science: Paris, 2004.

(2) Bryant, E. *Climate Process and Change*; Cambridge University Press: Cambridge, U.K., 1997.

(3) Damtoft, J. S.; Lukasik, J.; Herfort, D.; Sorrentino, D.; Gartner, E. M. *Cem. Concr. Res.* **2008**, *38*, 115−127.

(4) Taylor, H. F. W. *Cement Chemistry*, 2 ed.; Thomas Telford Publishing: London, 1997.

(5) Mindess, S.; Young, F. J.; Darwin, D. *Concrete*, 2 ed.; Prentice Hall: Upper Saddle River, NJ, 2003.

(6) Stephan, D.; Wistuba, S. *J. Eur. Ceram. Soc.* **2006**, *26*, 141−148.

(7) Sakurai, T.; Sato, T.; Yoshinaga, A. *5th ICCC*, Tokyo, Japan, 1969; Vol. *1*, pp 300−321.

(8) Maycock, J. N.; Skalny, J.; Kalyoncu, R. *Cem. Concr. Res.* **1974**, *4*, 835−847.

(9) Cuberos, A. J. M.; De la Torre, A. G.; Álvarez-Pinazo, G.; Martín-Sedeño, M. C.; Schollbach, K.; Pöllmann, H.; Aranda, M. A. G. *Environ. Sci. Technol.* **2010**, *44*, 6855−6862.

(10) Fierens, P.; Tirlocq, J. *Cem. Concr. Res.* **1983**, *13*, 267−276.

(11) De la Torre, A. G.; Bruque, S.; Cuberos, J. M.; Aranda, M. A. G. *Cem. Concr. Res.* **2008**, *38*, 1261−1269.

(12) Le Saoût, G.; Kocaba, V.; Scrivener, K. *Cem. Concr. Res.* **2011**, *41* (2), 133−148.

(13) Guinier, A.; Regourd M. *Proceedings of the 5th International Symposium on the Chemistry of Cement*; Tokyo, Japan, 1968; pp1.

(14) Dunstetter, F.; de Noirfontaine, M.-N.; Courtial, M. *Cem. Concr. Res.* **2006**, *36*, 39−53.

(15) Manzano, H.; Durgun, E.; Qomi, M. J. A.; Ulm, F.-J.; Pellenq, R. J. M.; Grossman, J. C. *Cryst. Growth Des.* **2011**, *11*, 2964−2972.

(16) Durgun, E.; Manzano, H.; Pellenq, R. J. M.; Grossman, J. C. *Chem. Mater.* **2012**, *24*, 1262−1267.

(17) Golovastikov, N. I.; Matveeva, R. G.; Belov, N. V. *Sov. Phys. Crystallogr.* **1975**, *20* (40), 441−445.

(18) Giannozzi, P.; et al. *J. Phys.: Condens. Matter* **2009**, *21*, 395502.

(19) Vanderbilt, D. *Phys. Rev. B* **1990**, *41*, 7892−7895.

(20) Perdew, J. P.; Chevary, J. A.; Vosko, S. H.; Jackson, K. A.; Pederson, M. R.; Singh, D. J.; Fiolhais, C. *Phys. Rev. B* **1992**, *46*, 6671−6687.

(21) Fletcher, R. *Practical Methods of Optimization*, 2 ed.; John Wiley & Sons: New York, 1987.

(22) Momma, K.; Izumi, F. *J. Appl. Crystallogr.* **2011**, *44*, 1272−1276.

(23) Hill, R. *Proc. Phys. Soc. A* **1952**, *65*, 349−354.

(24) Nye, J. F. *Physical Properties of Crystals: Their Representation by Tensors and Matrices*; Oxford University Press: New York, 1985.

(25) Momma, K.; Izumi, F. *J. Appl. Crystallogr.* **2011**, *44*, 1272−1276.

(26) Pickard, C. J.; Marui, F. *Phys. Rev. B* **2001**, *63*, 245101.

(27) Bak, M.; Rasmussen, J. T.; Nielsen, N. C. *J. Magn. Reson.* **2000**, *147*, 296−330.

(28) Jain, A.; Hautier, G.; Moore, C. J.; Ong, S. P.; Fisher, C. C.; Mueller, T.; Persson, K. A.; Ceder, G. *Comput. Mater. Sci.* **2011**, *50* (8), 2295−2310.

(29) Kubaschewski, O.; Alcock, C.; Spencer, P. *Materials Thermochemistry*, 6th ed.; Pergamom Press: Oxford, 1993.

(30) Hass, J. L., Jr.; Robinson, G. R., Jr.; Hemingway, B. S. *J. Phys. Chem. Ref. Data* **1981**, *10* (3), 575−669.

(31) Lukas, H. L.; Fries, S. G.; Sundman, B. *Computational Thermodynamics The Calphad Method*; Cambridge University Press: New York, 2007.

(32) Latfalla, S.; Shapovalov, V.; Bell, A. T. *J. Chem. Theory Comput.* **2011**, *7* (7), 2218−2223.

(33) Velez, K.; Maximilien, S.; Damidot, D.; Fantozzi, G.; Sorrentino, F. *Cem. Concr. Res.* **2001**, *31*, 555−561.

(34) Moudrakovski, I. L.; Alizadeh, R.; Beaudoin, J. J. *Phys. Chem. Chem. Phys.* **2012**, *12*, 6961−6969.

(35) Stephan, D.; Dikoundou, S. N.; Raudaschl-Sieber, G. *Mater. Struct.* **2008**, *41*, 1729−1740.

(36) Rejmak, P.; Dolado, J. S.; Stott, M. J.; Ayuela, A. *J. Phys. Chem. C* **2012**, *116*, 9755−9761.

(37) Birch, F. *J. Geophys. Res.* **1978**, *83*, 1257−68.

(38) Moon, J.; Yoon, S.; Wentzcovitch, R. M.; Clark, S. M.; Monteiro, P. J. M. *J. Am. Ceram. Soc.* **2012**, *95* (9), 2972−2978.

(39) Rollmann, G.; Rohrbach, A.; Entel, P.; Hafner, J. *Phys. Rev. B* **2004**, *69*, 165109.

(40) Liu, C. T.; Fu, C. L.; Chisholm, M. F.; Thompson, J. R.; Krcmar, M.; Wang, X.-L. *Prog. Mater. Sci.* **2007**, *52* (2−3), 352−370.

(41) Skibsted, J.; Jakobsen, H. J. J. *Chem. Soc. Faraday Trans.* **1994**, *90*, 2095−2098.

(42) Peterson, V. K.; Hunter, B. A.; Ray, A. *J. Am. Ceram. Soc.* **2004**, *87* (9), 1625−1634.

(43) Born, M. *J. Chem. Phys.* **1939**, *7*, 591−603.

(44) Bader, R. F. W. *Chem. Rev.* **1991**, *91*, 893−928.

(45) Lowdin, P.-O. *Adv. Quantum Chem.* **1970**, *5*, 185−199.

(46) De Proft, F.; Van Alsenoy, C.; Peeters, A.; Langenaeker, W.; Geerlings, P. *J. Comput. Chem.* **2002**, *23* (12), 1198−1209.

(47) Kumar, A.; Reed, J.; Sant, G. *J. Am. Ceram. Soc.* **2013**, *96* (9), 2766−2778.

(48) Valenti, G. L.; Sabatelli, V.; Marchese, B. *Cem. Concr. Res.* **1978**, *8*, 61−72.
(49) Medvedeva, J. E.; Teasley, E. N.; Hoffman, M. D. *Phys. Rev. B* **2007**, *76*, 155107.
(50) Burns, R. G. *Mineralogical Application of Crystal Field Theory*; Cambridge University Press: New York, 1970.
(51) Bullett, D. W. *J. Phys. C Solid State Phys.* **1983**, *16*, 2197−2207.